Strain-tunable magnetism at oxide domain walls

D. V. Christensen[1,7], Y. Frenkel[2,7], Y. Z. Chen [1], Y. W. Xie[3,4,5], Z. Y. Chen [3,4], Y. Hikita[3], A. Smith[1], L. Klein[6], H. Y. Hwang[3,4], N. Pryds [1]* and B. Kalisky [2]*

Applying stress to a ferroelastic material results in a nonlinear strain response as domains of different orientations mechanically switch. The ability to write, erase and move domain walls between such ferroelastic domains suggests a method for making nanoelectronics where the domain wall is the device. However, little is known about the magnetic properties of such domain walls. A fascinating model system is $SrTiO_3$, where the ferroelastic domain walls display strain-tunable polarity and enhanced conductivity. Here, we reveal a long-range magnetic order with modulations along the ferroelastic domain walls in $SrTiO_3$ and $SrTiO_3$-based heterointerfaces, which manifests itself as a striped pattern in scanning superconducting quantum interference device maps of the magnetic landscape. In conducting interfaces, the magnetism is coupled to itinerant electrons with clear signatures in magnetotransport measurements. The magnetic state is also coupled dynamically to the lattice and can be reversibly tuned by applying local external forces. This study raises the possibility of designing nanoscale devices based on domain walls where strain-tunable ferroelectric, ferroelastic and ferromagnetic orders may coexist.

n the search for properties beyond those found in pristine or doped materials, the coupling between the lattice and electronic degrees of freedom has proven particularly useful. Considering the case of the multifunctional oxide $SrTiO_3$ (STO), strain has led to a transition into ferroelectricity[1] and a 300% increase of the electron mobility[2]. Furthermore, where the lattice symmetry of the bulk STO crystal is broken, for example at the interface between $LaAlO_3$ (LAO) and STO, electrons can be confined to the interface, allowing a wide range of properties to be tuned by gating[3]. An additional intrinsic lattice symmetry breaking occurs below approximately 105 K, when the cubic unit cell of STO becomes tetragonal with the long axis oriented along the [001], [010] or [100] direction, thereby forming tetragonal domains with one of the three orientations[4–7]. The domain walls show modified electronic properties[8,9] and well-defined orientations that change when STO is subjected to thermal cycles above 105 K[8,10,11], mechanical forces[12,13] or electric fields[9,13], which enables regulation of the electronic properties of LAO/STO at the nanoscale.

A new dimension was added to the functionality of STO when magnetism was found in LAO/STO[14], as spin and its coupling to charge and lattice could then be utilized. Local imaging showed magnetic islands in LAO/STO with LAO thicknesses of at least 3 unit cells[15] where the magnitude and orientation of the magnetization could change in response to local stress[16]. However, the spin state of the confined electron gas turned out to display some intriguing scientific puzzles. First, the ferromagnetic order coexists with superconducting order even though ferromagnetism occurs by alignment of spins whereas electrons pair in a singlet state to form the conventional superconducting state[17,18]. Second, the superconductivity can be broken by application of a magnetic field, but the pairing of the electrons can survive in a non-superconducting state[19]. A recent experiment suggests that the electron pairing occurs at the ferroelastic domain walls[20], where they form a non-superconducting singlet state[19] or possibly even a spin-polarized

state with more than two paired electrons. The magnetic state and the electron pairing are therefore intimately linked[21].

Several theoretical models have been proposed to explain the magnetic state, including spiral magnetism in a charge-ordered state[22] and oxygen vacancy induced magnetism[23]. Experimentally, spatially resolved magnetometry measurements have played a key role. A scanning superconducting quantum interference device (SQUID) operating at low temperatures revealed disperse submicrometre ferromagnetic patches[15,17]. Room-temperature magnetic force microscopy was also used to probe the magnetic landscape emerging as the electrons at the LAO/STO interface were depleted using a top gate[24]. Additional experimental signatures of magnetism stem from (i) magnetometry measurements without spatial resolution, such as SQUID[25] & torque magnetometry[18], (ii) transport measurements reporting Kondo-like resistance minima[14,26], anomalous Hall effect[27–29] and negative or anisotropic magnetoresistance[25–28,30,31] and (iii) irradiation-based techniques such as β-decay from nuclear magnetic resonance[32] and X-ray magnetic circular dichroism[33]. On the other hand, a magnetic state was not consistently detected by scanning SQUID[15,34] or neutron reflectometry[35], and not only the nature of the magnetic state in these systems but even its mere existence is an open question.

Here, we observe a long-range magnetic order in LAO/STO, γ-Al_2O_3 (GAO)/STO and bare STO surfaces with striped modulations oriented parallel to the ferroelastic domain walls of STO. The magnetic state is coupled to the itinerant charges as well as the lattice, and it can be reversibly tuned by applying local external forces. This observation provides an opportunity for realizing multifunctional nanoelectronics at domain walls with strain-tunable ferromagnetic, ferroelastic and ferroelectric properties.

Imaging striped magnetic order

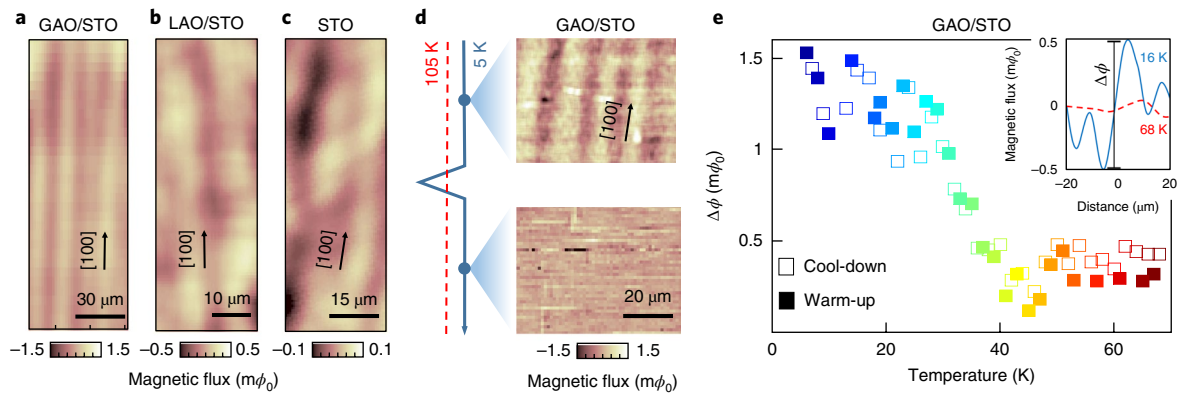We map the microscopic landscape of the magnetic state in STO-based systems using scanning SQUID microscopy

Fig. 1 | Scanning SQUID maps of striped magnetic order. a–c, Large-area scans showing magnetic stripes along the [100] crystallographic direction in GAO/STO, LAO/STO and vacuum-annealed STO. **d,** The same location on GAO/STO imaged in two subsequent scans before and after thermal cycling of the sample above 105 K. **e,** Temperature dependence of the peak-to-peak modulation amplitude ($\Delta\Phi$) defined using line scans (see inset) perpendicular to the stripes. The magnetic flux is offset by the average value of the scan for all figures.

(see Supplementary Section 1 for materials and methods). The scanning SQUID measures the magnetic flux entering a 1.8 μm wide pick-up loop, and produces a two-dimensional map of the flux when the pick-up loop scans across the sample surface. The measurements are performed in the absence of an externally applied magnetic field (background field < 0.1 μT) and therefore probe the magnetic field originating from a spontaneous magnetic order in the samples. In the case of LAO/STO, such measurements originally showed the presence of ferromagnetic patches in some of the samples[15]. Looking into regions without ferromagnetic patches and enhancing the signal-to-noise ratio, our magnetic flux maps reveal wide, striped modulations in LAO/STO, GAO/STO and vacuum-annealed STO (see Fig. 1a–c). The striped modulations extend over hundred micrometres, showing a long-range magnetic order. The striped modulations in the magnetic flux have been observed in five GAO/STO heterostructures with a typical magnitude of the order of 1 $m\Phi_0$ at 5 K. The modulations are generally stronger in GAO/STO when compared with LAO/STO and STO.

As the magnetic flux escaping a homogeneously magnetized sample will show a homogeneous flux map in regions far from the sample edges, the flux modulations that we observe point to a magnetization with spatial inhomogeneities. We estimate that the typical modulation magnitude of about 1 $m\Phi_0$ corresponds to changes in the magnetization of the order of 0.05 μ_B per surface unit cell (see Supplementary Section 2). The inhomogeneities are observed along the [100], [010], [110] and [1$\bar{1}$0] crystallographic directions of STO in all three material systems. These orientations coincide with the orientation of ferroelastic domain walls on the (001) surface of STO[5,9]. Furthermore, we can relate the magnetic stripes to STO crystallographic domain structure by performing temperature cycles around the structural transition temperature at 105 K. For example, in the case of GAO/STO we observe that a set of [100]-oriented striped magnetic modulations with an amplitude of 0.5 $m\Phi_0$ changes to barely detectable [110]-oriented modulations with an amplitude of less than 0.05 $m\Phi_0$ (see Fig. 1d). Changes in the striped magnetic landscape after thermal cycling also occur for bare STO without the GAO layer (see Supplementary Section 3). The results of the thermal cycling exclude the possibility that the magnetic stripes are caused by a trivial magnetic contamination.

Scanning SQUID has also been used to map the spatial distribution of current flow in LAO/STO[8] and GAO/STO[36], which revealed striped current modulations with the same crystallographic orientations as the magnetic stripes. Comparing the current flow with optical imaging of the domain structure showed that their orientations coincide[10]. Here, we perform magnetometry and current mapping on the same area, and observe a clear relation between the magnetic and current modulations (see Supplementary Section 4), implying that both the magnetic and current modulations are related to the domain structure.

When the temperature of the GAO/STO heterostructure is raised gradually from 5 K to 70 K, the magnetic modulations monotonically decrease in size until they disappear at around 40 K (see Fig. 1e). This characteristic temperature also roughly marks another anomaly of the STO substrate, where its quantum paraelectric behaviour causes the dielectric constant to diverge[37,38]. Other interesting observations below this temperature are polarity at the STO domain walls[39,40] and striped modulations in the current flow[8]. Cooling the heterostructure back to 5 K reintroduces the magnetic modulations without noticeable changes in size or location, as long as the 105 K transition temperature is not crossed.

Coupling between the magnetic state and current flow

The disappearance of the magnetic modulations above 40 K is reflected in the Hall and magnetoresistance measurements, as observed clearly in the case of GAO/STO. A Hall effect that is linear as a function of the magnetic field serves as a valuable tool for extracting the carrier density in a single-band conductor, while deviations from linearity can be used to deduce the band structure or magnetism. In the case of LAO/STO[41], the Hall resistance is S shaped at low temperatures for carrier densities exceeding about 1.7×10^{13} cm^{-2}. The S shape originates from transport occurring in two n-type bands with d_{xy} and d_{xz}/d_{yz} character[41]. The presence of magnetism can lead to the anomalous Hall effect, which has been observed as small perturbations to the S shape[27–29]. In the case of GAO/STO, the Hall resistance (R_{xy}) is linear for $T > 40$ K, revealing, for the sample presented in Fig. 2a, a high carrier density of $n_s \approx 6 \times 10^{14}$ cm^{-2}. For $T < 40$ K, pronounced nonlinearities arise without hysteresis. At these low temperatures, $|dR_{xy} / dB|$ increases at high magnetic fields, in contrast to the S-shaped nonlinearities observed in LAO/STO. If the nonlinearity of the Hall resistance in GAO/STO were due to two-band conductivity, it would entail the coexistence of a large number of electrons and holes, which we reject as detailed in Supplementary Section 5. Instead, we attribute the nonlinearity to the anomalous Hall effect resistance (R_{xy}^{AHE}) arising from the interaction between the itinerant electrons and the component of the magnetization normal to the interface[42], $R_{xy}^{AHE} = R_s^{AHE} M_z$. We find that the anomalous Hall prefactor (R_s^{AHE}) scales linearly with the sheet resistance (R_s), as expected when the skew scattering
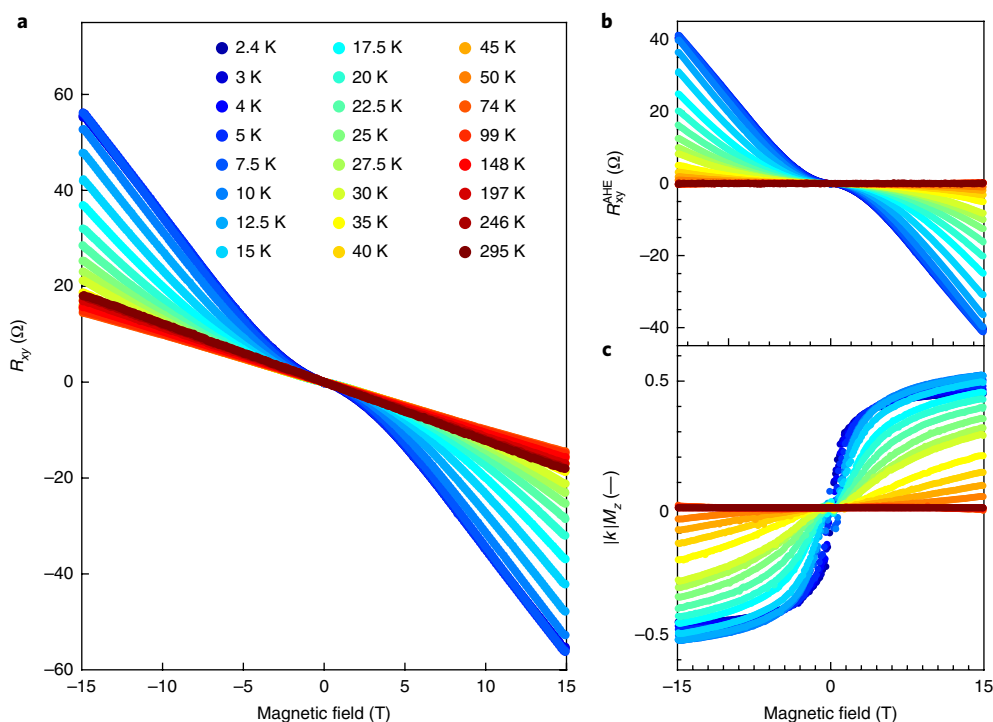
Fig. 2 | Anomalous Hall effect. a, Hall resistance (R_{xy}) as a function of the magnetic field applied perpendicular to the interface of GAO/STO. **b**, Anomalous Hall resistance (R_{xy}^{AHE}) obtained from R_{xy} by subtracting the ordinary Hall effect determined from the low-field slope of R_{xy}. **c**, The component of the magnetization perpendicular to the interface (M_z) multiplied by a proportionality constant k as described in the main text.

mechanism dominates[42] (see Supplementary Section 6). This leads to the following expression:

$$R_{xy} = R_{xy}^{OHE} + R_{xy}^{AHE} = -\frac{1}{en_s}B + kR_s(B,T)M_z(B,T)$$

where R_{xy}^{OHE} is the ordinary Hall effect and k is a field- and temperature-independent constant. For GAO/STO the d_{xy}/d_{yz} bands have been reported[43] to have comparable or even lower energy than d_{xy}. This, together with the high density of states of the d_{xy}/d_{yz} bands, means that the majority of the electrons are expected to populate the d_{xy}/d_{yz} bands. For simplicity we describe the ordinary Hall effect through the sheet carrier density (n_s) with a one-band model. Our data cannot exclude the presence of a second n-type band, but as outlined in Supplementary Section 6 this will not change the conclusions drawn here. At high magnetic fields, the sheet resistance increases linearly with the magnetic field, which results in a non-saturating anomalous Hall effect up to at least 15 T (see Fig. 2b). The usual extraction of the carrier density from the slope of the Hall resistance at high magnetic fields is therefore invalid, as this region includes contributions from both the ordinary and anomalous Hall effects. The carrier densities can be most accurately determined at low magnetic fields, where the contribution from the anomalous Hall effect is small (see Supplementary Section 6). The low-field slope of the Hall resistance is constant at all temperatures (see Fig. 2a), and we can therefore extract a temperature-independent carrier density of approximately $6 \times 10^{14}\,\text{cm}^{-2}$. This is consistent with the temperature-independent carrier density deduced optically from the infrared Berreman mode, similar to ref. [44].

By extracting $kM_z(B,T) = (R_{xy} - R_{xy}^{OHE})/R_s$ we infer that the component of the magnetization aligned with the perpendicular magnetic field starts to saturate at approximately 2 T for temperatures below approximately 8 K (see Fig. 2c). Increasing the temperature

opposes the alignment of magnetic moments up to $T \approx 40\,\text{K}$, where the magnetization is no longer detectable. This agrees well with the disappearance of the magnetic modulations observed with scanning SQUID. Together with the appearance of magnetic modulations and nonlinear Hall resistances for $T < 40\,\text{K}$, we also observe that the magnetoresistance deviates from Kohler's rule[45] at these temperatures (see Supplementary Section 7). This is consistent with the fact that Kohler's rule does not consider the reduction of charge-carrier scattering due to field-induced suppression of spin fluctuations. A similar behaviour of the Hall resistance and magnetoresistance is observed in four different samples (see Supplementary Section 6-7).

Mechanical tuning of the magnetic state
A particularly intriguing feature of the magnetic stripes is their tunability under small stresses. When applying a local force to GAO/STO, the temperature dependence of the magnetic modulations is markedly different (see Fig. 3a). Instead of the gradual decrease of the modulation strength observed up to 40 K, sharp, stripy features emerge when a force of 56 nN is applied. This applied force corresponds to a pressure of the order of $10^7\,\text{Pa}$ (see Methods). The features start to emerge around 10 K and the flux modulations are increased by a factor of four when 16 K is reached. Sharp features are only obtained after applying a local force to the sample surface with the tip of the sensor's chip, and the features become monotonically stronger when increasing the applied force (see Fig. 3b). Interestingly, in all cases, the original magnetic landscape without the sharp magnetic modulations can be restored without noticeable hysteresis by lowering the temperature or removing the force. Similar behaviour is also observed in LAO/STO (see Supplementary Section 8). We emphasize that this observation is different from the results of the same experiment performed on the ferromagnetic patches mentioned earlier[16], where the magnetization of the islands
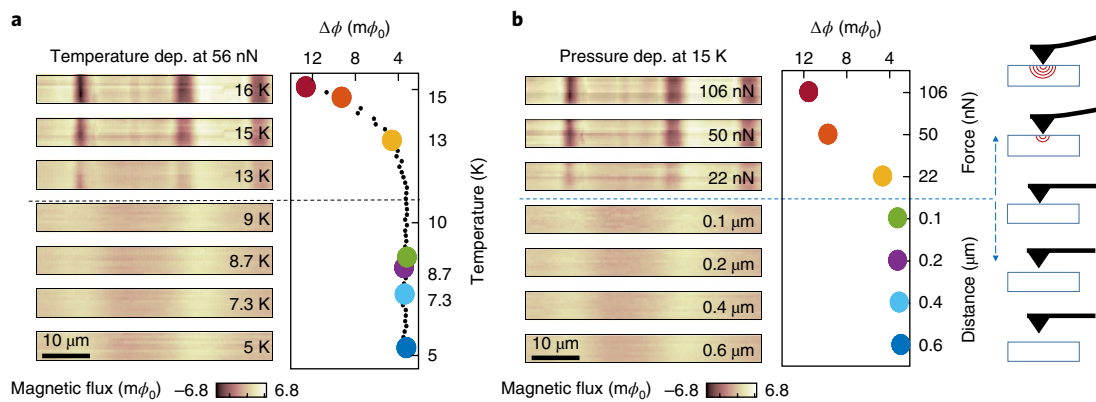
Fig. 3 | Pressure-dependent magnetic signal. a, Spatial modulation in the magnetic flux and the peak-to-peak modulation amplitude ($\Delta\Phi$) as a function of temperature obtained while pushing the tip of the SQUID into the GAO/STO sample with a force of 56 nN. **b**, Magnetic modulations at a fixed temperature of 15 K as the SQUID tip approaches the GAO/STO sample and creates a force on the sample surface. The force is measured capacitatively via the deflection of the SQUID cantilever. In all cases, the magnetic flux is offset by the average value of the scan.
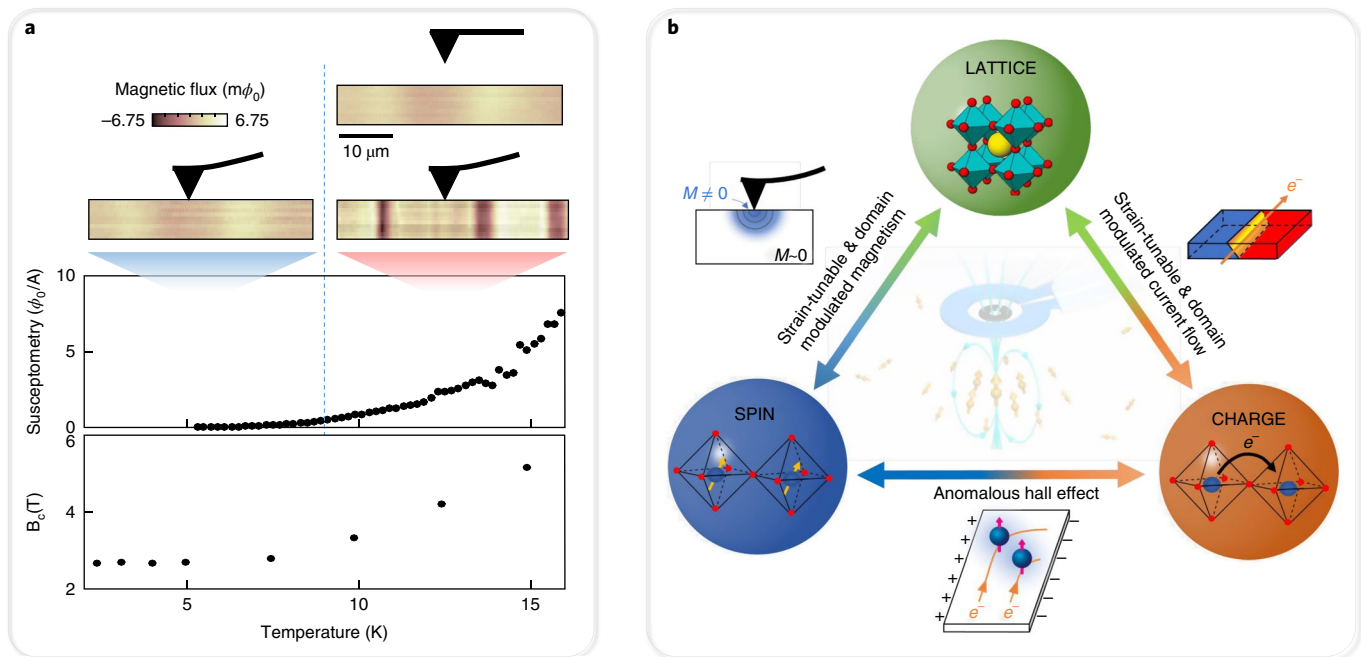

Fig. 4 | Coupling between lattice, spin and charge. a, Temperature dependence of the magnetic flux, the magnetic susceptibility and the characteristic field B_c, defined as the half width at half maximum of dR_{xy}/dB from Fig. 2a. **b**, A schematic illustration of the close coupling between the lattice, spin and charge degrees of freedom.

reoriented after application of local stress. The signal of the magnetic islands was almost two orders of magnitude stronger; they appeared in isolated and dispersed locations, and did not change with temperature[15]. The magnetic stripes we observe here are weaker, long range in nature, become stronger with temperature under the application of stress, and appear at different locations after temperature cycles. The relation between stress and magnetism can also be examined by investigating the naturally occurring stresses in the samples by mapping large areas. We find that areas with complex domain structures, formed to relieve local stress in the sample, are more likely to exhibit magnetic stripes (such as those in Fig. 1a–c). In the samples measured in this study, there were large areas with extents of hundreds of micrometres where no magnetic stripes were observed within our detection limit of 0.05 mΦ_0 (d.c.). After

temperature cycles above 105 K, magnetic stripes can be found within these areas, as in Fig. 2b. Modulations are observed more strongly in the vicinity of areas expected to exhibit stress, for example close to sample borders or around a scratch introduced intentionally on the surface of one sample.

Furthermore, we measured the magnetic response (susceptibility) by applying a small oscillating magnetic field of ±0.3 mT locally to the GAO/STO heterostructure while simultaneously applying a local force of 56 nN with the scanning probe. We find that the weak magnetic susceptibility observed below 5 K increases markedly above approximately 8 K (see Fig. 4a) and reaches a strong paramagnetic response up to 8 Φ_0/A at 16 K. The spatially resolved susceptibility data (Supplementary Section 9) reveal that the areas in Fig. 3 with strong magnetic signals also show a slower increase in the

paramagnetic susceptibility above approximately 8 K. Interestingly, this characteristic temperature also appears in the anomalous Hall effect analysis. The characteristic magnetic field (B_c) for the emergence of the anomalous Hall resistance can be described by the half width at half maximum of the bell-shaped dR_{xy}/dB. Below approximately 8K, the characteristic field is temperature independent, consistent with reports on NGO/STO[29], as expected if an exchange coupling in a magnetically ordered state prevents the magnetization from being induced or aligned along the field (see Fig. 4a). At higher temperatures, B_c is linearly increasing with temperature pointing towards a behaviour similar to paramagnetism where the alignment of magnetic moments is countered by thermal fluctuations.

Discussion

The striped magnetic modulations originate from the tetragonal domain structure of STO and are thus displayed in both STO and the STO-based heterostructures. The undoped STO studied here is electrically insulating, which hinders spintronic applications and investigation of the magnetic state through the anomalous Hall effect and magnetoresistance. Interfacing STO with GAO or LAO provides itinerant carriers to the surface of STO, which couple closely to the magnetic moments. Our observations uncover characteristic temperatures of approximately 8 K and 40 K occurring in both transport and SQUID measurements. We propose that these characteristic temperature regimes originate from the following factors.

(1) Below 8 K, the STO-based heterostructures are in a magnetically ordered state, which manifests itself in small or no modulations in the magnetization in the scanning SQUID maps (Fig. 3a,b). This state is characterized by a very weak (almost zero) susceptibility in response to small magnetic fields of ± 0.3 mT. Applying a magnetic field of $B_c \sim 2$ T aligns the magnetic moments perpendicular to the interface, which causes the anomalous Hall effect (Figs. 1a and 4a). At these temperatures, a local application of an external force of up to 106 nN has no observable effect on the ordered state.

(2) Above about 8 K, the magnetic order is less robust. This is supported by the increase in the paramagnetic susceptibility under a small applied force of 56 nN (Fig. 4a), suggesting a gradual change where ordered magnetic moments convert into paramagnetic moments. The conversion is slower at the domain walls, where the magnetic moments appear to be ordered more strongly, leading to areas with a slower growth in the magnetic susceptibility and large modulations of the magnetic signal (Supplementary Section 9). The alignment of the paramagnetic moments with the magnetic field is countered by thermal fluctuations, resulting in a linear increase of B_c with temperature (see Fig. 4a). The fragile magnetic order above 8 K is highly sensitive to externally applied forces, and stronger magnetic modulations can be induced here (Fig. 4a). This points towards a delicate balance between the unperturbed magnetic order existing in the absence of stress and a ferromagnetic order induced by the stress. Applying force causes a shift towards the ferromagnetic order in this temperature range. One of the possible mechanisms for the appearance of ferromagnetism is that the magnetic moments are produced by oxygen vacancies[23,46]. This is supported by the vast number of oxygen vacancies present particularly in GAO/STO[47–49] as well as the localized in-gap states formed by the oxygen vacancies[50].

The unperturbed magnetic order may be due to, for example, spiral magnetic ordering[22] or electron pairing[19,21] where it is expected that the state is non-hysteretic and results in a small magnetic susceptibility when applying small magnetic fields. It has been predicted that a pressure-sensitive transition from a spiral order to a ferromagnetic order occurs due to a polar distortion in STO where titanium ions are displaced relative to the oxygen ions[22]. This agrees well with recent experiments in LAO/STO showing that applying a local external force changes the polar state at the ferroelastic domain walls of STO[40]. Such a polarity-induced ferro-

magnetic order may also explain why the magnetic stripes (even in absence of an external force) are parallel to the domain walls in STO, as the domain walls have been observed to be polar[39,40].

(3) Above 40 K, all signatures of magnetism from the anomalous Hall effect, magnetoresistance and scanning SQUID vanish. This characteristic temperature also marks the disappearance of the striped current modulations in LAO/STO[8] as well as the disappearance of magnetism in LAO/STO according to some studies[30,31]. It also agrees reasonably well with the emergence of polar domain walls[39,40] only below approximately 50 K, again hinting towards the influence of STO polarity.

The advances made here demonstrate that STO-based material systems show an intriguing link between the charge, spin and lattice degrees of freedom in STO-based heterostructures as illustrated in Fig. 4b. The magnetic state couples to the current flow, causing an asymmetric scattering of the charge carriers (Fig. 2). The lattice and its domains also influence both the magnetic state (Fig. 1) and current flow[8,36,40]. In particular, applying an external pressure in vicinity of the ferroelastic domain walls dramatically alters the magnetic state (Fig. 3 and Supplementary Section 9), the current flow[40] and the polarity of the ferroelastic domain walls[40]. We therefore propose that an exciting multiferroic state awaits discovery, where a strain-tunable ferroelectric, ferroelastic and ferromagnetic order coexists. The key role played by the ferroelastic domain walls of STO demonstrates the prospects of using domain walls for functional nanoelectronics with tunable magnetic properties.

Data availability

The data that support the plots within this paper and other findings of this study are available from the corresponding authors upon reasonable request.

References

1. Haeni, J. H. et al. Room-temperature ferroelectricity in strained SrTiO$_3$. *Nature* **430**, 758–761 (2004).
2. Jalan, B., Allen, S. J., Beltz, G. E., Moetakef, P. & Stemmer, S. Enhancing the electron mobility of SrTiO$_3$ with strain. *Appl. Phys. Lett.* **98**, 132102 (2011).
3. Pai, Y.-Y., Tylan-Tyler, A., Irvin, P. & Levy, J. Physics of SrTiO$_3$-based heterostructures and nanostructures: a review. *Rep. Prog. Phys.* **81**, 036503 (2018).
4. Rimai, L. Electron paramagnetic resonance of trivalent gadolinium ions in strontium and barium titanates. *Phys. Rev.* **127**, 702–710 (1962).
5. Cowley, R. A. Lattice dynamics and phase transitions of strontium titanate. *Phys. Rev.* **134**, A981–A997 (1964).
6. Heidemann, A. & Wettengel, H. Die Messung der Gitterparameteränderung von SrTiO$_3$. *Z. Phys. Hadrons Nucl.* **258**, 429–438 (1973).
7. Lytle, F. W. X-ray diffractometry of low-temperature phase transformations in strontium titanate. *J. Appl. Phys.* **35**, 2212–2215 (1964).
8. Kalisky, B. et al. Locally enhanced conductivity due to the tetragonal domain structure in LaAlO$_3$/SrTiO$_3$ heterointerfaces. *Nat. Mater.* **12**, 1091–1095 (2013).
9. Honig, M. et al. Local electrostatic imaging of striped domain order in LaAlO$_3$/SrTiO$_3$. *Nat. Mater.* **12**, 1112–1118 (2013).
10. Erlich, Z. et al. Optical study of tetragonal domains in LaAlO$_3$/SrTiO$_3$. *J. Supercond. Nov. Magn.* **28**, 1017–1020 (2015).
11. Frenkel, Y. et al. Anisotropic transport at the LaAlO$_3$/SrTiO$_3$ interface explained by microscopic imaging of channel-flow over SrTiO$_3$ domains. *ACS Appl. Mater. Interfaces* **8**, 12514–12519 (2016).
12. Chang, T. S. Domain structure of SrTiO$_3$ under uniaxial stresses. *J. Appl. Phys.* **43**, 3591–3595 (1972).
13. Sidoruk, J. et al. Quantitative determination of domain distribution in SrTiO$_3$—competing effects of applied electric field and mechanical stress. *J. Phys. Condens. Matter* **22**, 235903 (2010).
14. Brinkman, A. et al. Magnetic effects at the interface between non-magnetic oxides. *Nat. Mater.* **6**, 493–496 (2007).
15. Kalisky, B. et al. Critical thickness for ferromagnetism in LaAlO$_3$/SrTiO$_3$ heterostructures. *Nat. Commun.* **3**, 922 (2012).
16. Kalisky, B. et al. Scanning probe manipulation of magnetism at the LaAlO$_3$/SrTiO$_3$ heterointerface. *Nano Lett.* **12**, 4055–4059 (2012).
17. Bert, J. A. et al. Direct imaging of the coexistence of ferromagnetism and superconductivity at the LaAlO$_3$/SrTiO$_3$ interface. *Nat. Phys.* **7**, 767–771 (2011).

18. Li, L., Richter, C., Mannhart, J. & Ashoori, R. C. Coexistence of magnetic order and two-dimensional superconductivity at LaAlO$_3$/SrTiO$_3$ interfaces. *Nat. Phys.* **7**, 762–766 (2011).

19. Cheng, G. et al. Electron pairing without superconductivity. *Nature* **521**, 196–199 (2015).

20. Pai, Y.-Y. et al. One-dimensional nature of pairing and superconductivity at the SrTiO$_3$/LaAlO$_3$ interface. *Phys. Rev. Lett.* **120**, 147001 (2018).

21. Pai, Y.-Y., Tylan-Tyler, A., Irvin, P. & Levy, J. LaAlO$_3$/SrTiO$_3$: a tale of two magnetisms. Preprint at https://arxiv.org/abs/1610.00789 (2016).

22. Banerjee, S., Erten, O. & Randeria, M. Ferromagnetic exchange, spin-orbit coupling and spiral magnetism at the LaAlO$_3$/SrTiO$_3$ interface. *Nat. Phys.* **9**, 626–630 (2013).

23. Pavlenko, N., Kopp, T., Tsymbal, E. Y., Sawatzky, G. A. & Mannhart, J. Magnetic and superconducting phases at the LaAlO$_3$/SrTiO$_3$ interface: the role of interfacial Ti 3d electrons. *Phys. Rev. B* **85**, 020407 (2012).

24. Bi, F. et al. Room-temperature electronically-controlled ferromagnetism at the LaAlO$_3$/SrTiO$_3$ interface. *Nat. Commun.* **5**, 5019 (2014).

25. Ariando et al. Electronic phase separation at the LaAlO$_3$/SrTiO$_3$ interface. *Nat. Commun.* **2**, 188 (2011).

26. Hu, H.-L. et al. Subtle interplay between localized magnetic moments and itinerant electrons in LaAlO$_3$/SrTiO$_3$ heterostructures. *ACS Appl. Mater. Interfaces* **8**, 13630–13636 (2016).

27. Joshua, A., Ruhman, J., Pecker, S., Altman, E. & Ilani, S. Gate-tunable polarized phase of two-dimensional electrons at the LaAlO$_3$/SrTiO$_3$ interface. *Proc. Natl Acad. Sci. USA* **110**, 9633–9638 (2013).

28. Seri, S., Schultz, M. & Klein, L. Interplay between sheet resistance increase and magnetotransport properties in LaAlO$_3$/SrTiO$_3$. *Phys. Rev. B* **86**, 085118 (2012).

29. Gunkel, F. et al. Defect control of conventional and anomalous electron transport at complex oxide interfaces. *Phys. Rev. X* **6**, 031035 (2016).

30. Ben Shalom, M. et al. Anisotropic magnetotransport at the SrTiO$_3$/LaAlO$_3$ interface. *Phys. Rev. B* **80**, 140403 (2009).

31. Wang, X. et al. Magnetoresistance of two-dimensional and three-dimensional electron gas in LaAlO$_3$/SrTiO$_3$ heterostructures: influence of magnetic ordering, interface scattering, and dimensionality. *Phys. Rev. B* **84**, 075312 (2011).

32. Salman, Z. et al. Nature of weak magnetism in SrTiO$_3$/LaAlO$_3$ multilayers. *Phys. Rev. Lett.* **109**, 257207 (2012).

33. Lee, J.-S. et al. Titanium d$_{xy}$ ferromagnetism at the LaAlO$_3$/SrTiO$_3$ interface. *Nat. Mater.* **12**, 703–706 (2013).

34. Wijnands, T. *Scanning Superconducting Quantum Interference Device Microscopy: Sensitive Mapping of Magnetic Flux on Thin Films.* PhD thesis, Univ. Twente (2013).

35. Fitzsimmons, M. R. et al. Upper limit to magnetism in LaAlO$_3$/SrTiO$_3$ heterostructures. *Phys. Rev. Lett.* **107**, 217201 (2011).

36. Christensen, D. V. et al. Electron mobility in γ-Al$_2$O$_3$/SrTiO$_3$. *Phys. Rev. Appl.* **9**, 054004 (2018).

37. Neville, R. C., Hoeneisen, B. & Mead, C. A. Permittivity of strontium titanate. *J. Appl. Phys.* **43**, 2124–2131 (1972).

38. Rowley, S. E. et al. Ferroelectric quantum criticality. *Nat. Phys.* **10**, 367–372 (2014).

39. Scott, J. F., Salje, E. K. H. & Carpenter, M. A. Domain wall damping and elastic softening in SrTiO$_3$: evidence for polar twin walls. *Phys. Rev. Lett.* **109**, 187601 (2012).

40. Frenkel, Y. et al. Imaging and tuning polarity at SrTiO$_3$ domain walls. *Nat. Mater.* **16**, 1203–1208 (2017).

41. Joshua, A., Pecker, S., Ruhman, J., Altman, E. & Ilani, S. A universal critical density underlying the physics of electrons at the LaAlO$_3$/SrTiO$_3$ interface. *Nat. Commun.* **3**, 1129 (2012).

42. Nagaosa, N., Sinova, J., Onoda, S., MacDonald, A. H. & Ong, N. P. Anomalous Hall effect. *Rev. Mod. Phys.* **82**, 1539–1592 (2010).

43. Cao, Y. et al. Anomalous orbital structure in a spinel–perovskite interface. *npj Quantum Mater.* **1**, 16009 (2016).

44. Yazdi-Rizi, M. et al. Infrared ellipsometry study of the confined electrons in a high-mobility γ-Al$_2$O$_3$/SrTiO$_3$ heterostructure. *Europhys. Lett.* **113**, 47005 (2016).

45. Pippard, A. B. *Magnetoresistance in Metals* (Cambridge Univ. Press, New York, 1989).

46. Coey, J. M. D., Venkatesan, M. & Stamenov, P. Surface magnetism of strontium titanate. *J. Phys. Condens. Matter* **28**, 485001 (2016).

47. Chen, Y. Z. et al. A high-mobility two-dimensional electron gas at the spinel/perovskite interface of γ-Al$_2$O$_3$/SrTiO$_3$. *Nat. Commun.* **4**, 1371 (2013).

48. Christensen, D. V. et al. Controlling the carrier density of SrTiO$_3$-based heterostructures with annealing. *Adv. Electron. Mater.* **3**, 1700026 (2017).

49. Gunkel, F. et al. Thermodynamic ground states of complex oxide heterointerfaces. *ACS Appl. Mater. Interfaces* **9**, 1086–1092 (2017).

50. Schütz, P. et al. Microscopic origin of the mobility enhancement at a spinel/perovskite oxide heterointerface revealed by photoemission spectroscopy. *Phys. Rev. B* **96**, 161409 (2017).

Acknowledgements

Author contributions

D.V.C., Y.F., N.P. and B.K. initiated this work. D.V.C. performed the transport measurements and prepared the GAO/STO samples. Y.W.X., Z.Y.C., Y.H. and H.Y.H. prepared the LAO/STO samples. D.V.C., Y.F. and B.K. performed the scanning SQUID measurements. D.V.C. and Y.F. performed data analysis. D.V.C., Y.F., A.S., Y.Z.C., L.K., N.P. and B.K. interpreted the data. D.V.C. wrote the manuscript with Y.F. and input from all authors.

Competing interests

The authors declare no competing interests.

Additional information